SUPPLEMENTARY INFORMATION

doi:10.1038/nature11596

1 Spatial distribution of the excitations without rotational alignment

Here we show the spatial distribution of excitations based on the same data as in Fig. 2b and 2c of the main text but without the rotational alignment procedure described in the Methods section.

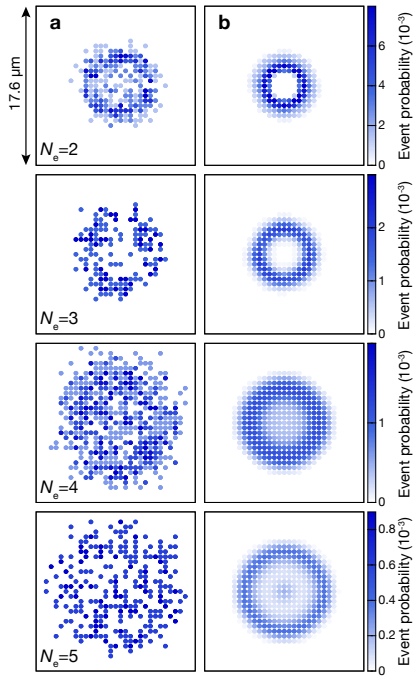

Supplementary Figure 1 | Spatial distribution of the distribution of excitations before rotation. **a**, Histograms constructed from the experimental data. The Rydberg atoms are excited with higher probability close to the edge than in the centre of the cloud. The resulting ring-shaped excitation region is clearly visible for $N_e = 2$ and 3. The contrast decreases for $N_e = 4$ and 5 due to the lower number of occurences in the experiment. **b**, Theoretical predictions for the excitation from initial clouds of same temperature and atom number as in the experiment (see Fig. 2 for details).

2 Spatially resolved analysis of the excitation dynamics

The coherence of the dynamics can be revealed in a more obvious way by studying the time evolution of the spatial distribution of the Rydberg excitations. For this purpose, we considered the subset of microscopic configurations with only one excitation. Because the blockade radius is only slightly smaller than the system diameter, only those configurations in which the excitation is located close to the edge of the system are significantly coupled to configurations with two excitations. This results in different time constants for the dynamics at different distance r from the centre. We have investigated this effect theoretically by calculating the time evolution of the relative probability for the excitation to be located close to the centre of the system (green line in Fig. S2). In contrast to Fig. 4 of the main text, we now observe Rabi-like oscillations with notable amplitude over long timescales. We performed the corresponding measurement in the experiment for two pulse durations (blue circles) and find reasonable agreement. This provides further evidence for the coherence of the many-body dynamics in the experiment.

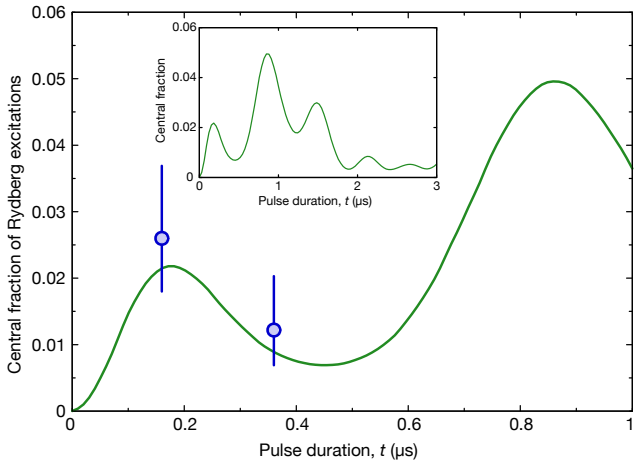

Supplementary Figure 2 | Excitation dynamics at the centre of the system. Relative number of excitations in the central nine sites as a function of the excitation pulse duration for microscopic configurations with a single excitation $N_e = 1$. The theoretical calculation (green line, inset) reveals the coherent evolution, which is hardly visible in the time evolution of the total excitation number. Two experimental points (blue circles) were obtained from an additional dataset containing about 800 images per pulse duration. It was characterized by the temperature of the initial state $T = 9(2)\,\mathrm{nK}$, the atom number $N_{at} = 210(30)$ and the radius $R = 4.2(5)\,\mu\mathrm{m}$. These experimental parameters were included in the numerical simulation. The error bars denote one standard deviation of the mean (s.e.m.).

3 Additional information on the datasets

The experimental data results from three different datasets (A, B and C). Each dataset was characterized by a temperature, T, atom number, N_{at}, and diameter, $2R$, which we extracted from a fit to the ground state atom distribution in the initial state[1] (Table 1). The datasets A and B were used for Fig. 2 and 3, while the dataset C was used for Fig. 4. The distribution of the number of excitations in the datasets A and B is detailed in Table 2, where we also indicated which subset of images was used for which figures. The dataset C consisted of 54 images per pulse duration and the relative distribution of excitations is directly visible in Fig. 4.

	dataset A	dataset B	dataset C
T (nK)	8(4)	13(2)	9(4)
N_{at}	150(30)	390(30)	150(30)
R (µm)	3.6(4)	5.4(4)	3.6(4)

Supplementary Table 1 | Temperature T, atom number N_{at} and radius R for the datasets A, B and C. Errors, s.d.

	dataset A		dataset B	
number of excitations	number of images	figures	number of images	figures
0	177	–	321	–
1	235	–	375	3a
2	191	2a, 3b	390	3a
3	65	2a, 3b	308	3a
4	7	–	177	2a, 3a, 3b
5	1	–	64	2a, 3a, 3b
6	0	–	14	–
7	0	–	5	–

Supplementary Table 2 | Distribution of the number of excitations in the datasets A and B. For each subset of images we have also indicated in which figure of the main text it has been used.

4 Numerical calculations

In order to determine the dynamics governed by the Hamiltonian in Eq. (1), we expand the many-body wave function, $|\psi\rangle$, of the N_{at}-atom system in terms of Fock-states

$$|\psi\rangle = c^{(0)}|0\rangle + \sum_{\boldsymbol{i}_1} c^{(1)}_{\boldsymbol{i}_1}|\boldsymbol{i}_1\rangle + \sum_{\boldsymbol{i}_1,\boldsymbol{i}_2} c^{(2)}_{\boldsymbol{i}_1,\boldsymbol{i}_2}|\boldsymbol{i}_1,\boldsymbol{i}_2\rangle + \ldots + \sum_{\boldsymbol{i}_1,\ldots,\boldsymbol{i}_{N_{\mathrm{at}}}} c^{(N_{\mathrm{at}})}_{\boldsymbol{i}_1,\ldots,\boldsymbol{i}_{N_{\mathrm{at}}}}|\boldsymbol{i}_1,\ldots,\boldsymbol{i}_{N_{\mathrm{at}}}\rangle\ , \quad \text{(S1)}$$

where $|\boldsymbol{i}_1,\ldots,\boldsymbol{i}_{N_{\mathrm{e}}}\rangle$ corresponds to a state with N_e Rydberg excitations located at lattice sites $\boldsymbol{i}_1$ to $\boldsymbol{i}_{N_{\mathrm{e}}}$, and $c^{(N_{\mathrm{e}})}_{\boldsymbol{i}_1,\ldots,\boldsymbol{i}_{N_{\mathrm{e}}}}$ denotes the respective time dependent amplitude. The basis states are eigenfunctions of the Hamiltonian (1) in the absence of laser driving, with energy eigenvalues $E^{(N_{\mathrm{e}})}_{\boldsymbol{i}_1,\ldots,\boldsymbol{i}_{N_{\mathrm{e}}}} = \sum_{\alpha<\beta}^{N_{\mathrm{e}}} V_{\boldsymbol{i}_\alpha \boldsymbol{i}_\beta}$. For a system of N_{at} atoms, this basis set expansion yields a set of $2^{N_{\mathrm{at}}}$ coupled differential equations (Fig. S3). Due to the exponential growth of the number of many-body states with N_{at}, a direct

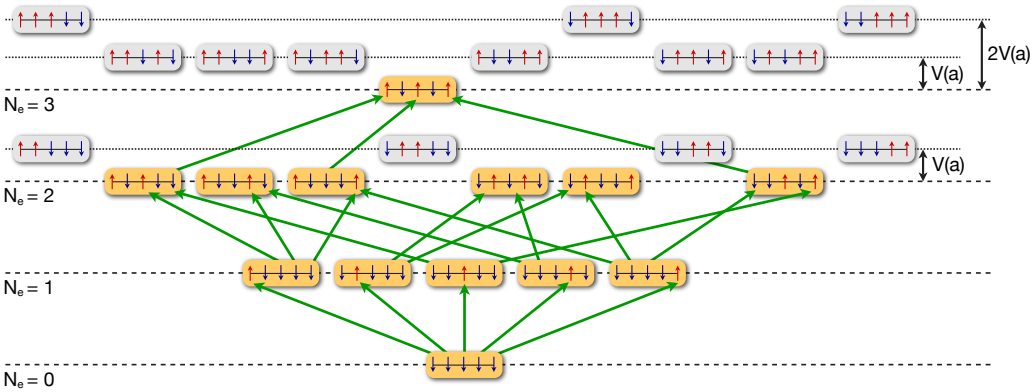

Supplementary Figure 3 | Schematics of the numerical calculations. The underlying many-body level structure is shown for the example of a one-dimensional chain of five atoms. The atomic states are symbolised by effective spins, with spin-down (blue arrows) and spin-up (red arrows) corresponding to the atomic ground and Rydberg state, respectively. In the displayed example, we consider strong interactions $V(a) \gg \hbar\Omega$ between adjacent Rydberg excitations, while next-nearest neighbour interactions $V(2a) = V(a)/64 < \hbar\Omega$ are assumed to be smaller than the laser coupling strength. Consequently, the dynamics of near resonant basis states (orange boxes) is explicitly calculated in the simulations, while strongly shifted states (grey boxes) do not participate in the excitation dynamics and are discarded (see text for further details). The near-resonant laser coupling between relevant many-body states is indicated by the green arrows. Due to the strong geometrical constraint imposed by the interaction blockade combined with the finite system size, many-body states containing more than $N_{\mathrm{e}} = 3$ Rydberg excitations do not need to be considered.

numerical propagation is practically impossible for the large number of atoms in our experiments, $N_{\mathrm{at}} \sim 100$. In order to make the calculations feasible, we exploit the blockade effect and discard all many-body states containing Rydberg atom pairs separated by less than a critical distance R_{c}. For the present simulations, we obtain well-converged results for $R_{\mathrm{c}} \simeq R_{\mathrm{b}}/2$, where R_{b} is the blockade radius. The resulting geometric constraint not only reduces the number of relevant many-body states within a given N_{e}-manifold, but, due to the finite system size, also restricts the total number of excitations N_{e} necessary to obtain converged results. For the parameters considered in this work, a maximum number of Rydberg excitations of ${N_{\mathrm{e}}}^{(\mathrm{max})} = 6$ was found sufficient. This procedure allows to significantly mitigate the otherwise strong exponential scaling of the underlying Hilbert space dimension, and yields a power-law dependence $\sim N_{\mathrm{at}}^{N_{\mathrm{e}}^{(\mathrm{max})}}$ of the number of relevant basis states on the total number of atoms. This makes the computations feasible, albeit still demanding, for such large systems as in our experiment.

5 Optical detection scheme

We developed a fully-optical detection technique for Rydberg atoms, which represents an alternative to the usual detection schemes based on the ionisation of Rydberg atoms[2–5]. Here, we provide additional details to those given in the main text, especially regarding the detection efficiency and spatial resolution.

5.1 Stimulated deexcitation of the Rydberg atoms

We stimulated the Rydberg atoms down to the ground state by resonantly driving the $|43S_{1/2}, m_J = -1/2\rangle \rightarrow |5P_{3/2}, F = 3, m_F = -3\rangle$ transition. The Rabi frequency associated with this resonant single-photon transition was typically several MHz. In combination with the short lifetime of the $5P_{3/2}$ state (27 ns), this allows for a very efficient and fast ($< 2\,\mu$s) pumping to the ground state. The laser light resonant with the transition between the Rydberg and the intermediate states was produced by a resonant electro-optical modulator (EOM) in the path of the excitation laser at 480 nm, which created a sideband at the desired intermediate-state detuning $\delta/(2\pi) = 742$ MHz. The other sideband and the carrier have negligible influence on the atoms in the deexcitation phase since they are off-resonant. The EOM also allows for the required fast switching of the deexcitation light within $< 1\,\mu$s.

5.2 Spatial resolution

Two effects can in principle limit the spatial resolution of our detection technique. The first one is the residual hopping of the atoms during the fluorescence imaging phase. We found that such an event can occur in our experiment with a probability of approximately 1 % per particle. When this happens, the moving atom will yield a fluorescence signal on two adjacent sites, which can be falsely attributed to two distinct atoms by the reconstruction algorithm. This detection artifact results in a correlation signal at short distances $r < 1\,\mu\text{m}$ (Fig. 3a). However, due to their rarity these events have negligible influence on the spatial resolution. The second effect is the possible motion of the Rydberg atoms in the optical lattice potential before the imaging phase. For Rydberg atoms, the lattice potential has similar amplitude but opposite sign compared to ground state atoms[6]. An excited atom therefore finds itself at a maximum of the periodic potential and can move in the xy-plane with an average velocity of $\sim 30\,\text{nm}/\mu\text{s}$, for a typical depth of the optical lattice potential of $V_{\text{lat}} = 40\,E_{\text{r}}$. Both effects lead to a possible motion of the Rydberg atoms by about one lattice site during the 10 µs of the removal pulse. The recoil velocity acquired in the two-photon excitation process is insignificant in comparison as it is oriented along z-direction and only of smaller magnitude $\simeq 4\,\text{nm}/\mu\text{s}$.

5.3 Detection efficiency

The detection efficiency for Rydberg atoms in our setup is limited by the lifetime of the Rydberg state and by the anti-confining character of the optical lattice potential for the Rydberg atoms. If a Rydberg atom decays to the ground state during the removal pulse, it will be removed as well and not detected. The residual motion of the Rydberg atoms in the lattice potential also leads to a reduction of the detection efficiency when the atoms move away from the focal plane of the imaging system, which has a depth of focus of order 1 µm. Both effects can be reduced by minimising the time the atoms spend in the Rydberg state after the excitation pulse, by reducing the duration of the removal pulse for the ground state atoms. A removal pulse duration of 10 µs turned out to offer the best compromise between a good detection efficiency of Rydberg atoms and a low survival probability of ground state atoms.

We estimated the detection efficiency in three different ways. First, we measured the lifetime of the atoms in the Rydberg state in the lattice by varying the duration of the removal pulse. We fitted a $1/e$-decay time $\tau = 25(5)\,\mu\text{s}$, which corresponds to a detection efficiency of 65(5) %. A second estimation is provided by the time evolution of the number of Rydberg excitation displayed in Fig. 4. Here the theoretical

prediction matches the data best when assuming a detection efficiency of $\sim 75\,\%$, which is compatible with the previous estimate. Finally, the statistical weight of the different number of excitations can also be related to the detection efficiency. This last estimation points to a higher detection efficiency of $\sim 80\,\%$. Combining all these values with equal weight, we finally obtain a detection efficiency of $75\,\%$ with an uncertainty of about $10\,\%$.

6 Validity of the the model

The validity of the Hamiltonian in Eq. (1) for our experimental system relies on two main assumptions, which are discussed in this section: the positions of the atoms is frozen during the dynamics and all decoherence sources can be neglected.

6.1 Movement of the atoms during the dynamics

The ground state atoms were confined in a three-dimensional optical lattice of depth $V_{xy} = 40(3)\,E_\mathrm{r}$ in the xy-plane and $V_z = 75(5)\,E_\mathrm{r}$ along the z-axis, where $E_\mathrm{r} = (2\pi\hbar)^2/(8ma_\mathrm{lat}^2)$ denotes the recoil energy of the lattice, and m the atomic mass of ^{87}Rb. For the minimum lattice depth used in the experiment of $V_\mathrm{lat} = 40\,E_\mathrm{r}$, the time associated to the inverse of the tunnelling matrix element was $\hbar/J \simeq 700\,\mathrm{ms}$, and therefore negligible compared to the timescale of the internal dynamics. The Rydberg atoms move in the lattice potential with a typical velocity of $30\,\mathrm{nm/\mu s}$ (see discussion in Section 5.2), which can also be neglected.

6.2 Light scattering from the intermediate state

One source of decoherence in our experimental system is light scattering from the intermediate state used in the two-photon excitation process. The laser beam off-resonantly driving the ground-to-intermediate-state transition had a detuning of $742\,\mathrm{MHz}$ and an intensity of $\sim 450\,\mathrm{mW/cm^2}$, yielding a scattering rate of $9 \times 10^4\,\mathrm{s^{-1}}$. This corresponds to a coherence time of $11\,\mu\mathrm{s}$, which is a factor of ten longer than the typical timescale of the many-body dynamics.

6.3 Laser linewidth

The finite spectral width of the optical radiation driving the transition to the Rydberg state acts as a decoherence source and was reduced by carefully stabilising

the frequency of the excitation lasers. We could achieve a two-photon linewidth of $\approx 70\,\mathrm{kHz}$, leading to a coherence time of $14\,\mu\mathrm{s}$. Technical details on the laser setup are provided in Section 7.

6.4 Two-photon Rabi frequency

We determined the two-photon Rabi frequency by driving Rabi oscillation in a very dilute system, where the average distance between two atoms was larger than the blockade radius of the $43S$ state, for which the van der Waals coefficient is $C_6 = -1.6 \times 10^{-60}\,\mathrm{J\,m^6}$ [ref. 7]. The measurement was very time-consuming in our experimental setup since at such densities only a few atoms are located within the waist of the excitation lasers, resulting in a very low signal (about one Rydberg excitation per image) with relatively large fluctuations. We could observe one period of the Rabi oscillation, as expected from the combined coherence time of light scattering and laser linewidth of $6\,\mu\mathrm{s}$, and extracted from the data a Rabi frequency of $\Omega/(2\pi) = 170(20)\,\mathrm{kHz}$.

The waists of the two laser beams of wavelength 780 nm and 480 nm [ref. 8] driving the two-photon transition were $57(2)\,\mu\mathrm{m}$ and $17(5)\,\mu\mathrm{m}$, respectively. The largest systems we studied had a radius of $5.4\,\mu\mathrm{m}$, leading to a variation in the coupling strength to the Rydberg state by $< 20\,\%$ over the whole system.

7 Laser setup

The light at a wavelength of 780 nm was produced by a diode laser whose frequency was stabilised using a modulation transfer spectroscopy in a rubidium vapour cell. The light at 480 nm was generated by frequency-doubling light at 960 nm, which was emitted from a diode laser and amplified by a tampered amplifier. This second laser was stabilised by a phase-lock to a master laser, which allows for tuning its frequency while maintaining the narrow laser linewidth. The master laser at 960 nm was locked to a temperature stabilised ULE cavity in a vacuum chamber. The short-term linewidth of both excitation lasers was measured using an independent resonator (EagleEye, Sirah Laser- und Plasmatechnik GmbH, Germany), which can resolve linewidths down to $\sim 20\,\mathrm{kHz}$. We obtained a linewidth of 20 kHz for the laser at 480 nm and 50 kHz for the laser at 780 nm. We measured the long-term stability of the two-photon excitation to be 50 kHz over several hours (FWHM of the centre of the line) using EIT-spectroscopy in a rubidium vapour cell[9].

References

1. Sherson, J. F. *et al.* Single-atom-resolved fluorescence imaging of an atomic Mott insulator. *Nature* **467,** 68–72 (2010).
2. Löw, R. *et al.* An experimental and theoretical guide to strongly interacting Rydberg gases. *J. Phys. B – At. Mol. Opt.* **45,** 113001 (2012).
3. Schwarzkopf, A., Sapiro, R. & Raithel, G. Imaging Spatial Correlations of Rydberg Excitations in Cold Atom Clouds. *Phys. Rev. Lett.* **107,** 103001 (2011).
4. Urban, E. *et al.* Observation of Rydberg blockade between two atoms. *Nature Phys.* **5,** 110–114 (2009).
5. Potvliege, R. M. & Adams, C. S. Photo-ionization in far-off-resonance optical lattices. *New J. Phys.* **8,** 163 (2006).
6. Anderson, S., Younge, K. & Raithel, G. Trapping Rydberg Atoms in an Optical Lattice. *Phys. Rev. Lett.* **107,** 263001 (2011).
7. Singer, K., Stanojevic, J., Weidemüller, M. & Côté, R. Long-range interactions between alkali Rydberg atom pairs correlated to the ns–ns, np–np and nd–nd asymptotes. *J. Phys. B – At. Mol. Opt.* **38,** S295–S307 (2005).
8. Mack, M. *et al.* Measurement of absolute transition frequencies of ^{87}Rb to nS and nD Rydberg states by means of electromagnetically induced transparency. *Phys. Rev. A* **83,** 052515 (2011).
9. Mohapatra, A. K., Jackson, T. R. & Adams, C. S. Coherent Optical Detection of Highly Excited Rydberg States Using Electromagnetically Induced Transparency. *Phys. Rev. Lett.* **98,** 113003 (2007).